RSC Advances

PAPER

View Article Online
View Journal | View Issue

Cite this: *RSC Adv.*, 2017, **7**, 36374

$K_3LaTe_2O_9$:Er: a novel green up-conversion luminescence material†

Hong Wang, Xiumei Yin, Mingming Xing, Yao Fu, Ying Tian,* Xin Feng, Tao Jiang and Xixian Luo*

A novel green up-conversion luminescence material, $K_3LaTe_2O_9$:Er, was synthesised *via* a solid-state reaction method. $K_3LaTe_2O_9$:Er phosphors were characterised by X-ray diffraction, reflectance spectroscopy, Raman spectroscopy, photoluminescence spectroscopy, up-conversion spectroscopy and temperature sensing performance analysis. The diffraction pattern of the hexagonal $K_3LaTe_2O_9$:0.02Er microcrystals was indexed with Miller indices and the lattice constants were $a = b = 0.60636 \pm 0.00018$ nm, and $c = 1.49543 \pm 0.00037$ nm. The photoluminescence under 380 nm excitation and the up-conversion luminescence under 980 and 1550 nm pumping were investigated. The influence of Er^{3+} ion concentration and excitation power on the luminescence properties of $K_3LaTe_2O_9$:Er was also discussed. $K_3LaTe_2O_9$:Er phosphor presented green down-shifting emission and up-conversion luminescence under 380, and 980 nm excitation and yellow–green up-conversion luminescence under 1550 nm pumping, respectively, and the red emission component was enhanced with the increment in excitation wavelength. The quenching concentration of Er^{3+} ions in $K_3LaTe_2O_9$:Er was much higher than that in normal phosphors. This result can be attributed to the suppression of energy migration because the shortest (0.606 nm) and average distance (0.9720 nm) between Er^{3+} ions were significantly large in $K_3LaTe_2O_9$. Therefore, the electric quadrupole–quadrupole interactions between Er^{3+} ions are the dominant energy transfer process in down-shift emission, and the UCL mechanism can be regarded as the excited state absorption in $K_3LaTe_2O_9$:Er. Furthermore, the doping concentration of Er^{3+} ions influenced the temperature sensitivity of $K_3LaTe_2O_9$:Er.

Received 3rd June 2017
Accepted 17th July 2017

DOI: 10.1039/c7ra06191a

rsc.li/rsc-advances

1. Introduction

Rare-earth (RE)-doped luminescence materials play an important role in illumination, display, temperature sensor, security and biomedicine.[1–3] Selecting appropriate materials with excellent luminescence performance based on practical applications is important. In general, the luminescence properties of phosphors are regulated through the selection of matrix materials. Matrix materials can bond doped RE ions, and the symmetry and strength of the crystal field exert significant effects on the optical properties of RE ions. Moreover, the practical applications of matrix materials are largely dependent on their physicochemical properties.

Tellurates with rich chemical structures and unique physical properties have attracted considerable attention. RE-doped tellurite glass with relatively low phonon energy, high reflection index, and excellent thermal stability has become a popular research topic.[4–7] However, tellurate phosphors have seldom been reported. For instance, Sobczyk *et al.*[8] studied the optical properties of $Y_2Te_4O_{11}:Sm^{3+}$. Zhang *et al.*[9] investigated the structure and luminescence properties of $Li_3Y_3Te_2O_{12}:Eu^{3+}$.

$K_3LaTe_2O_9$ is a new quaternary tellurite material with medium phonon energy.[10] In the present work, the diffraction pattern of $K_3LaTe_2O_9$ microcrystals was indexed with Miller indices. The down-shifting luminescence (DSL, $\lambda_{em} = 380$ nm) and up-conversion luminescence (UCL, $\lambda_{em} = 980$ and 1550 nm) of $K_3LaTe_2O_9$:Er were reported for the first time. In addition, the thermal quenching and temperature sensor of $K_3LaTe_2O_9$:Er were investigated.

2. Experimental

2.1 Sample preparation

$K_3LaTe_2O_9$:Er phosphors were synthesized *via* the solid-state reaction method. The starting raw materials La_2O_3 (99.99%), Er_2O_3 (99.99%), K_2CO_3 (A. R.), and TeO_2 (A. R.) were weighed according to stoichiometric ratio. Secondly, the above-mentioned materials were thoroughly mixed and ground using an agate ball mill for 20 min. Finally, all samples were sintered at 650 °C for 5 h. $K_3LaTe_2O_9$:*x*Er samples with different Er^{3+} concentrations were then obtained ($x = 0$, 2, 8, 14, 20, 26, 32, 38, 44 mol%).

Physics Department, Dalian Maritime University, Dalian, Liaoning 116026, PR China. E-mail: tianying15@hotmail.com; luoxixiandl@126.com; Fax: +86 411 84723626; Tel: +86 411 84723626

† Electronic supplementary information (ESI) available. See DOI: 10.1039/c7ra06191a

2.2 Characterisation technique

X-ray powder diffraction was performed at 40 kV and 40 mA from 10° to 70° using a SHIMADZU-6000 X-ray generator with Cu Kα ($\lambda = 0.154184$ nm) radiation. The DSL and UCL spectra (400 nm to 900 nm) were recorded on a Hitachi F-4600 fluorescence spectrophotometer equipped with a power-tunable 980 and 1550 nm fibre laser diode (LD). The highest available power for the LD was approximately 800 and 700 mW, respectively. The beam of the LD was focused by the convex lens before measurement. The temperature dependence of the DSL spectra was tested by a self-assembly temperature control system with a XMT-4000 programmable temperature controller. The reflection spectra of the samples were obtained with a UV-3600 SHIMADZU UV-Vis-NIR spectrophotometer. The maximum phonon energy of the $K_3LaTe_2O_9$ host lattice was obtained by a micro-Raman spectroscope (Jobin Yvon HR800, excited by 633 nm He–Ne laser with a laser spot size of 1 μm^2, in line mapping mode). The scanning electron microscope (SEM) and Energy Dispersive Spectrometer (EDS) of the sample were obtained by JEOL-6360LV field emission gun scanning electron microscopy. The X-ray photoelectron spectroscopy (XPS) spectrum of the sample was obtained by ESCALAB250 surface analysis system.

3. Results and discussion

Fig. 1a shows the XRD pattern of the $K_3LaTe_2O_9$:0.02Er sample. The diffraction peaks of the present sample are similar to those in ref. 10, indicating that the hexagonal $K_3LaTe_2O_9$:0.02Er was synthesised. The micrograph and EDS of the $K_3LaTe_2O_9$ crystal shown in Fig. S1.† The concentration of element in the K_3LaTe_2O crystal shown in Table S1.† The molar ratio of K, La, Te, and O element is 3.0 : 1 : 2.1 : 7.7 (Table S1†). The diffraction peaks in the XPS pattern are assigned to K^+, O^{2-}, Te^{6+}, and La^{3+}, respectively (Fig. S2†). The relative concentration values calculated by elemental sensitivity factor method of K, O, Te, and La atoms are 61.88, 18.47, 12.31, and 7.34%, respectively, which are close to the theoretical calculated values in the $K_3LaTe_2O_9$. However, the standard PDF data of $K_3LaTe_2O_9$:Er are not available, and ref. 10 did not provide the index data of $K_3LaTe_2O_9$. The lattice parameters of $K_3LaTe_2O_9$:0.02Er were calculated by the least square method in accordance with the data in Table S2,† and the crystal lattice parameters of the $K_3LaTe_2O_9$:0.02Er sample were obtained: $a = b = 0.60636 \pm 0.00018$ nm, $c = 1.49543 \pm 0.00037$ nm, $V = 0.47617$ nm^3. $K_3LaTe_2O_9$ is a 3D framework structure (Fig. 1b). K atoms are two sites that coordinate with nine and twelve O atoms forming distorted cuboctahedra, respectively. Te atoms are linked to six O atoms to form $[TeO_6]$ octahedral, and two $[TeO_6]$ octahedral are connected to form a face-sharing $[Te_2O_9]^{6-}$ anion group. La atoms are surrounded by six O atoms in regular octahedra, and La^{3+} ions have a high-ordered state in the crystal lattice.

Fig. 2 shows the Raman spectrum of the $K_3LaTe_2O_9$:0.02Er sample. The peaks situated at 285, 415, 667, 718, and 832 cm^{-1} corresponding to the $K_3LaTe_2O_9$ host shown in ref. 10. Singh[11] reported that the range of 500–580 cm^{-1}, 620–680 cm^{-1}, and 780–900 cm^{-1} are the characteristic peaks of Er^{3+} ion. Therefore, several peaks (remarked as *) are related to Er^{3+} ions. Some weak peaks in Raman spectrum are also observed due to defects

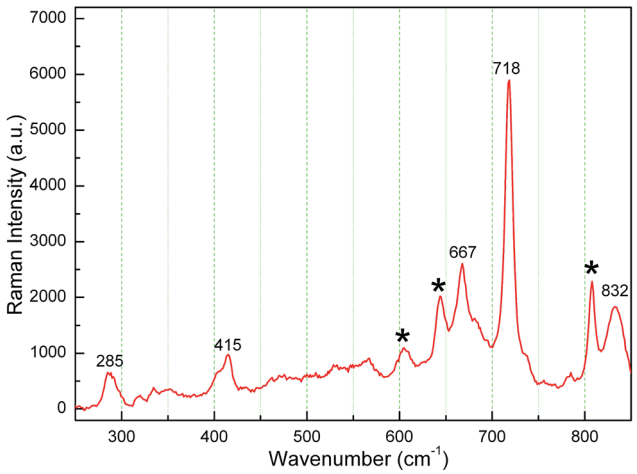

Fig. 2 Raman spectrum of the $K_3LaTe_2O_9$:0.02Er sample.

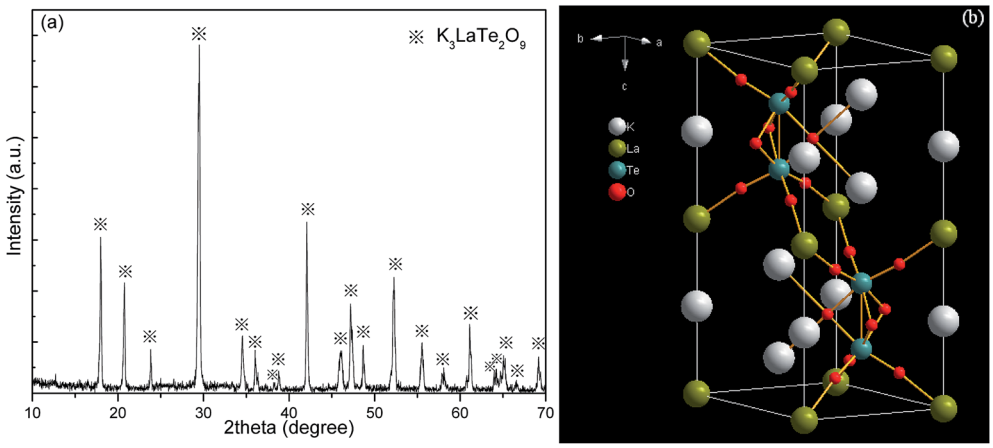

Fig. 1 XRD pattern (a) and crystal structure diagram (b) of $K_3LaTe_2O_9$:0.02Er.

in the lattice of $K_3LaTe_2O_9$:Er.[12] Raman peaks shift to the right side, which results from Er^{3+} doping. The maximum phonon energy of the $K_3LaTe_2O_9$ host lattice is $\hbar\omega = 832\ cm^{-1}$. Thus, $K_3LaTe_2O_9$ with an appropriate phonon energy can be considered as an alternative for the luminescence host material.

Fig. 3 shows the diffuse reflectance spectra of $K_3LaTe_2O_9$:xEr (x = 2, 26, 44 mol%). As shown in the figure, the absorption peaks become stronger with increasing Er^{3+} ion concentration. The absorption peaks at 380, 409, 486, 525, 550, 653, 798, 973, and 1537 nm can be assigned to transition from an Er^{3+} ground state $^5I_{15/2}$ to excited states $^2K_{15/2}$, $^2H_{9/2}$, $^4F_{7/2}$, $^2H_{11/2}$, $^4S_{3/2}$, $^4F_{9/2}$, $^4I_{9/2}$, $^4I_{11/2}$, and $^4I_{13/2}$ levels. The $^4I_{13/2}$ level of Er^{3+} ions has a strong absorption to 980 nm photons. The absorption efficiency of the $^4I_{13/2}$ level of Er^{3+} ions to 1550 nm photons reached 89% of the 1537 nm. Therefore, Er^{3+} ions can be effectively sensitised by 1550 nm exciting light. The absorption edge of $K_3LaTe_2O_9$:Er can be obtained in absorption spectra. The reflectance spectra of $K_3LaTe_2O_9$:Er was converted into the absorption spectra based on the Kubelka–Munk formula[13] (inset in Fig. 3):

$$F(R) = (1 - R)^2/2R = K/S, \quad (1)$$

where R is the reflectance, K is the absorption coefficient, and S is the scattering coefficient. The absorption edges of $K_3LaTe_2O_9$:xEr are 287, 293 and 301 nm, which correspond to the band gap energies of 4.32, 4.23, and 4.12 eV, respectively (x = 2, 26, 44 mol%). The band gap value decreases with increasing Er^{3+} ion concentration. This phenomenon can be attributed to the fact that the ionic radii of Er^{3+} (0.088 nm) are smaller than that of La^{3+} (0.102 nm), thus resulting in the shrinkage of the lattice matrix and the red shift of the absorption bands after doping Er^{3+} ions.

Fig. 4a shows the excitation and DSL spectra of $K_3LaTe_2O_9$:Er. The excitation spectrum of $K_3LaTe_2O_9$:Er presents a strong peak at ~380 nm, which corresponds to the $^4G_{11/2} \rightarrow {}^4I_{15/2}$ transition by monitoring the 550 nm emission of Er^{3+} ions. $K_3LaTe_2O_9$:Er under 380 nm excitation ($K_3LaTe_2O_9$:Er at 380 nm) exhibits pure

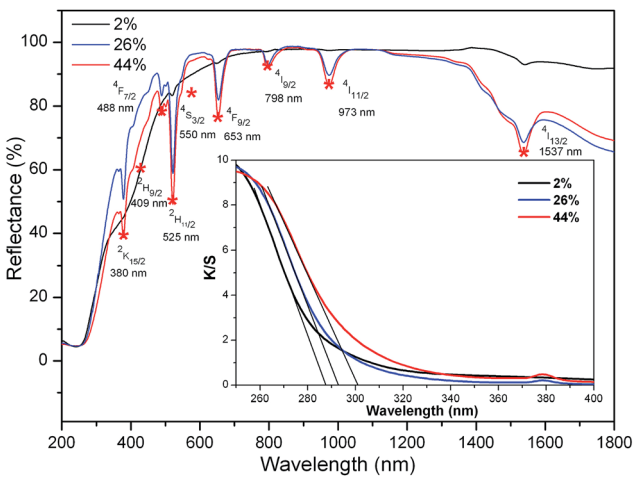

Fig. 3 UV-Vis-NIR reflectance and absorption (inset) spectra of $K_3LaTe_2O_9$:xEr (x = 2, 26, 44 mol%).

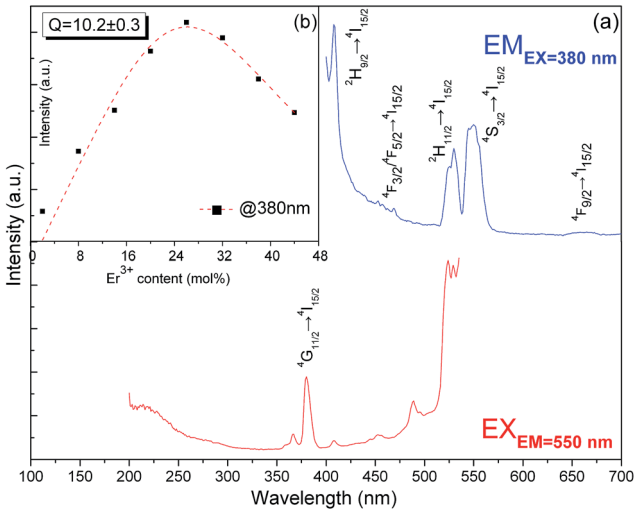

Fig. 4 Excitation and DSL spectra of $K_3LaTe_2O_9$:Er (a) and dependence of $^2H_{11/2}/^4S_{3/2} \rightarrow {}^4I_{15/2}$ green DSL integrated intensity on Er^{3+} ion concentration (b).

green emission (I_G, $^2H_{11/2}/^4S_{3/2} \rightarrow {}^4I_{15/2}$), and the red irradiation (I_R, $^4F_{9/2} \rightarrow {}^4I_{15/2}$) is very weak with the green and red fluorescence intensity ratio (I_G/I_R) I_G/I_R = 21.3. $K_3LaTe_2O_9$:Er at 380 nm has a relatively strong peak at ~410 nm, which is assigned to the $^4H_{9/2} \rightarrow {}^4I_{15/2}$ transition of Er^{3+} ions. In addition, the emission spectra present a weak band located at 450–470 nm, which corresponds to the $^4F_{3/2}/^4F_{5/2} \rightarrow {}^4I_{15/2}$ transition. The doping concentration of the optimum Er^{3+} ions is 26 mol% (Fig. 4b). The integrated intensity initially increases with increasing doping concentration, reaches its maximum at around 26 mol%, and then decreases. The quenching concentration is much higher than that of conventional materials.[14] The relationship between the DSL intensity and doping concentration of the luminescence centre can be described by the Van Uitert model.[15]

$$I(C) = C/\kappa(1 + \beta C^{Q/3}), \quad (2)$$

where C is the concentration of RE^{3+} ions, κ and β are the constants and Q is the interaction types between RE^{3+} ions. Q = 3, 6, 8, and 10 is related to exchange interaction, electric dipole–dipole (D–D), electric dipole–quadrupole (D–Q), and electric quadrupole–quadrupole (Q–Q) interactions. Eqn (2) was fitted to the data in Fig. 4b, and the Q value of $K_3LaTe_2O_9$:Er at 380 nm is 10.2 ± 0.3 ≈ 10. Therefore, the Q–Q interaction between Er^{3+} ions is dominant for quenching $^2H_{11/2}/^4S_{3/2}$ levels in $K_3LaTe_2O_9$:Er. However, ET is usually caused by the D–D interaction in most materials.[16]

The shortest distance between La^{3+}–La^{3+} ions is 0.606 nm in the $K_3LaTe_2O_9$ matrix, which is significantly larger than that of Y^{3+}–Y^{3+} in Y_2O_3 (0.351 nm). The average distance $\bar{d}$ between doping Er^{3+} ions can be expressed as[17]

$$\bar{d} = \left(\frac{V}{xZ}\right)^{1/3}, \quad (3)$$

where V is the volume of the unit crystal cell, x is the Er^{3+} doping concentration and Z is the number of molecules in the unit crystal cells. When the Er^{3+} ion concentration is 26 mol%, $\bar{d} = 0.9711$ nm, which is also significantly larger than that in Gd_2O_2S:10% Er^{3+} (0.753 nm) and β-$NaYF_4$:25% Er^{3+} (0.663 nm).[17] Therefore, the shortest distance and average distance between Er^{3+} ions are large in the $K_3LaTe_2O_9$ matrix. The energy migration is affected by matrix.[18] The $K_3LaTe_2O_9$ host can provide long lattice sites for Er^{3+} ions, which is helpful in obtaining heavy dopes and effectively reduces the harmful ET process. Moreover, it is beneficial in improving the absorption of incident light.

Under 980 nm pumping, $K_3LaTe_2O_9$:Er presents the green UCL ($K_3LaTe_2O_9$:Er at 980 nm) (inset of Fig. 5a). The UCL spectra for $K_3LaTe_2O_9$:xEr at 980 nm are shown in Fig. 5a ($x = 2$, 8, 14, 20, 26, 32, 44 mol%). The spectra consist of basically two groups in the visual regions at an interval of 500–800 nm: (1) the strongest green emission at ~525 nm and ~550 nm can be attributed to the joint contributions of the Er^{3+} ion $^2H_{11/2} \rightarrow {}^4I_{15/2}$ and $^4S_{3/2} \rightarrow {}^4I_{15/2}$ transition, and (2) the second strongest red emission at ~665 nm can be attributed to the Er^{3+} ion $^4F_{9/2} \rightarrow {}^4I_{15/2}$ transition. The emission peaks intensity of $K_3LaTe_2O_9$:Er at 980 nm are successively enhanced with increasing concentration of Er^{3+} ions. The concentration quenching phenomenon is not observed when the concentration of Er^{3+} ion reaches 44 mol%. Compared with the DSL spectra in Fig. 4a, the red emission is improved significantly, and its I_G/I_R ratio is reduced from 21.3 (DSL) to 2.5–4.7 (UCL, 980 nm). The luminescence colour can be tuned by the doping concentration of Er^{3+} ions and the excitation power under 980 nm excitation. As the Er^{3+} ion concentration continues to increase from 2 mol% to 38 mol%, the red light component is enhanced, and its I_G/I_R ratio is reduced from 3.9 to 2.7. By contrast, the green component can be effectively enhanced and the I_G/I_R ratio is increased from 2.5 to 4.7 with increasing excitation power (Fig. 5e). Under high excitation power pumping, more photons can be absorbed by Er^{3+} ions, which results in Er^{3+} ions populating high levels easily.

In addition, the dependence of luminescence-integrated intensity on the Er^{3+} ion concentration of $K_3LaTe_2O_9$:Er at 980 nm is nearly linear when the concentration is low (2–26 mol%), which indicates that the UCL mechanism can be

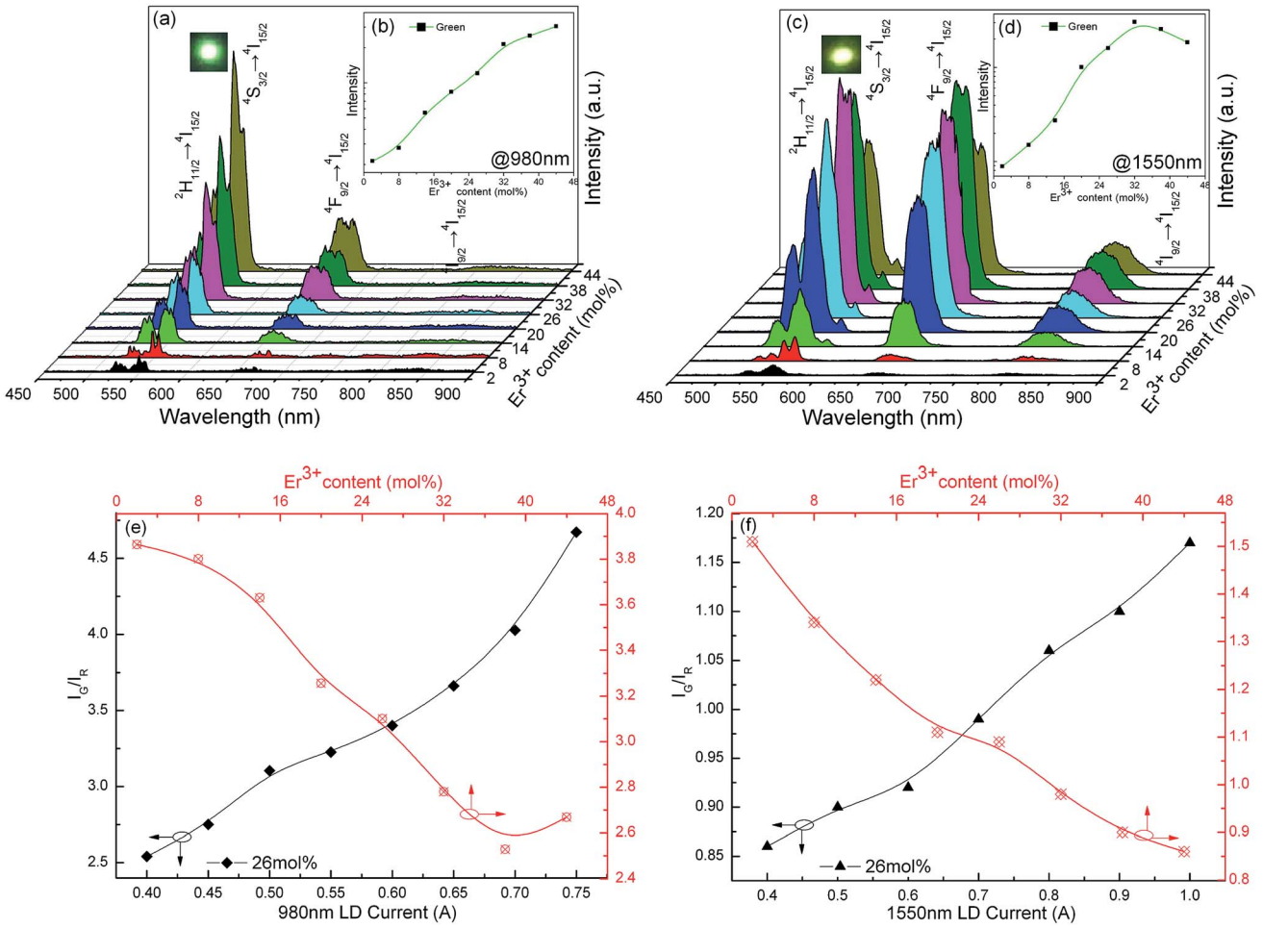

Fig. 5 UCL spectra of the $K_3LaTe_2O_9$:xEr sample under 980 nm (a) and 1550 nm (c) pumping, the dependence of the green UCL intensity on Er^{3+} doping concentration under 980 nm (b) and 1550 nm (d) pumping and the dependence of the I_G/I_R value of the $K_3LaTe_2O_9$:xEr sample on Er^{3+} doping concentration and pumping current under 980 nm (e) and 1550 nm (f) excitation ($x = 2$, 8, 14, 20, 26, 32, 38, 44 mol%).

regarded as excited state absorption (ESA). This phenomenon is owed to the long distance between the RE ions in the $K_3LaTe_2O_9$ structure resulting in the suppression of the ET.[19] $K_3LaTe_2O_9$:Er at 980 nm presents an approximate nonlinear relation when Er^{3+} > 26 mol%, indicating that the ET between Er^{3+} ion pairs also plays an important role in the UC process (Fig. 5b).

$K_3LaTe_2O_9$:Er exhibits yellow–green emission under 1550 excitation ($K_3LaTe_2O_9$:Er at 1550 nm) (inset of Fig. 5b). The UCL spectra in the visible region of $K_3LaTe_2O_9$:Er at 1550 nm have the same peak positions and shape with different relative intensities compared with those at 980 nm excitation. However, the red emission intensity is significantly improved excited by 1550 nm, and its I_G/I_R ratio is reduced to 0.86–1.17. Whilst a relatively strong NIR emission peak at ~800 nm is observed, the optimum doping concentration of Er^{3+} ions is 32 mol% at 1550 nm pumping (Fig. 5c). When the Er^{3+} ion concentration is increased from 2 mol% to 44 mol%, the I_G/I_R ratio is reduced from 1.5 to 0.86. On the contrary, the green emission can be significantly enhanced, and the I_G/I_R ratio is increased from 0.86 to 1.17 with increasing excitation power (Fig. 5f). The UCL mechanism of $K_3LaTe_2O_9$:Er at 1550 nm is mainly based on the ESA process when the concentration of Er^{3+} ions is less than 16 mol%. Subsequently, the ET process begins to dominate (Er^{3+} > 16 mol%, Fig. 5d). Compared with DSL, the red component of $K_3LaTe_2O_9$:Er is increased, particularly under 1550 nm pumping. However, the red UCL mechanism is still controversial.[20,21]

The non-radiation multiphonon relaxation rate (ω_P) between the energy levels of RE ions can be expressed using the Miyakawa–Dexter theory:[22,23]

$$\omega_P = \omega_0 \exp\left(-\frac{\alpha \Delta E}{\hbar\omega}\right), \quad (4)$$

where α, and ω_0 are the constants related to the host properties, ΔE is the energy gap (cm^{-1}) and $\hbar\omega$ is the maximum phonon energy of the host lattice.

The energy gaps of $^4S_{3/2}$–$^4F_{9/2}$ and $^4I_{11/2}$–$^4I_{13/2}$ are $\Delta E \approx 2980$ and 3400 cm^{-1}, corresponding to $\Delta E/\hbar\omega = 3.6$ and 4.1. The strong green emission ($^2H_{11/2}/^4S_{3/2} \rightarrow {}^4I_{15/2}$) and almost no red emission ($^4F_{9/2} \rightarrow {}^4I_{15/2}$) of $K_3LaTe_2O_9$:Er at 380 nm are observed directly excited at 380 nm, indicating that the non-radiative relaxation $^4S_{3/2} \rightarrow {}^4F_{9/2}$ is weak (Fig. 4a). However, the non-radiative relaxation probability of $^4I_{11/2} \rightarrow {}^4I_{13/2}$ is smaller than that of the $^4S_{3/2} \rightarrow {}^4F_{9/2}$, that is, the $^4S_{3/2} \rightarrow {}^4F_{9/2}$ non-radiative relaxation process is not the main reason for the red UCL in $K_3LaTe_2O_9$:Er at 980 nm. Therefore, the mechanism of red intensity enhancement can only be the cross relaxation (CR) between Er^{3+} ions. The red emission intensity is very weak even at high Er^{3+} concentrations for DSL because the CR between Er^{3+} ions is restrained in $K_3LaTe_2O_9$ owing to the joint contributions of the long distance between the RE ions and the lack of intermediate metastable energy level below the $^4S_{3/2}$ level. However, the long-level lifetime of the intermediate levels is inspired, and the CR processes significantly enhance the red emission in the UCL compared with DSL. The short-level lifetime of the $^4I_{9/2}$ level and the small energy gap of $^4I_{9/2}$–$^4I_{11/2}$ ($\Delta E \approx 1950$ cm^{-1}, $\Delta E/\hbar\omega = 2.3$) are the major factors influencing the red radiation enhancement of $K_3LaTe_2O_9$:Er at 1550 nm.[24,25] Therefore, the difference in UCL spectra and quenching concentration for DSL and UCL results mainly from the different energy level population of the Er^{3+} ions caused by the different excitation routes.

The different optimum Er^{3+} concentrations of $K_3LaTe_2O_9$ under various wavelengths pumping is caused by the different excitation paths, level lifetime, and absorption cross section of levels. The transition model of the Er^{3+} ions in the $K_3LaTe_2O_9$ phosphor excited at 380, 980, and 1550 nm is established to describe the luminescence process in Fig. 6. Red emission ($^4F_{9/2} \rightarrow {}^4I_{15/2}$) of Er^{3+} ions was very weak in the DSL spectrum under 380 nm pumping (Fig. 4a). The green UCL process for $K_3LaTe_2O_9$:Er at 380 nm is as follows: $^4I_{15/2} + h\nu_{980\ nm} \rightarrow {}^4G_{11/2}$, $^4G_{11/2} \rightarrow {}^4H_{9/2}$ + multiphonon relaxation + $h\nu_{410\ nm}$, $^4H_{9/2} \rightarrow {}^4F_{3/2}/{}^4F_{5/2}$ + multiphonon relaxation + $h\nu_{450–470\ nm}$, $^4F_{3/2}/{}^4F_{5/2} \rightarrow {}^2H_{11/2}/{}^4S_{3/2}$ + multiphonon relaxation, $^2H_{11/2}/{}^4S_{3/2} \rightarrow {}^4I_{15/2} + h\nu_{525\ nm}/h\nu_{550\ nm}$. The green UCL process for $K_3LaTe_2O_9$:Er at 980 nm is as follows: $^4I_{15/2} + h\nu_{980\ nm} \rightarrow {}^2I_{11/2}$, $^4I_{11/2} + h\nu_{980\ nm} \rightarrow {}^4F_{7/2}$, $^4F_{7/2} \rightarrow {}^2H_{11/2}/{}^4S_{3/2}$ + multiphonon relaxation, and $^2H_{11/2}/{}^4S_{3/2} \rightarrow {}^4I_{15/2} + h\nu_{525\ nm}/h\nu_{550\ nm}$. Its red UCL mechanism is the $^4F_{7/2} + {}^4I_{11/2} \rightarrow {}^4F_{9/2} + {}^4F_{9/2}$ CR process. The red and NIR intensity of $K_3LaTe_2O_9$:Er at 1550 nm is significantly enhanced. The UCL mechanism is as follows: $^4I_{15/2} + h\nu_{1550\ nm} \rightarrow {}^2I_{13/2}$, $^4I_{13/2} + h\nu_{1550\ nm} \rightarrow {}^4I_{9/2}$, $^4I_{9/2} + h\nu_{1550\ nm} \rightarrow {}^2H_{11/2}$, $^4I_{9/2}$ + multiphonon relaxation $\rightarrow {}^4I_{11/2}$, $^4I_{11/2} + h\nu_{1550\ nm} \rightarrow {}^4F_{9/2}$, and $^4F_{9/2} \rightarrow {}^4I_{15/2} + h\nu_{660\ nm}$, $^4I_{9/2} \rightarrow {}^4I_{15/2} + h\nu_{800\ nm}$.

As shown in Fig. 7a, the $K_3LaTe_2O_9$:0.26Er sample can nearly recover to its original intensity after cooling down to room temperature from 473 K, indicating that $K_3LaTe_2O_9$:Er phosphors have a high resistance to heating damage by using a 380 nm xenon lamp as the excitation source. Fig. 7b shows the integrated intensities of $K_3LaTe_2O_9$:*x*Er phosphors as a function of temperature. The integrated emission intensities are normalized at room temperature for $K_3LaTe_2O_9$:*x*Er (x = 20, 26, 32 mol%). With the successive increase in the heating temperature, the green UCL intensity of different concentration samples gradually decreases. At 473 K, the integrated intensity of the $K_3LaTe_2O_9$:*x*Er (x = 20, 26, 32 mol%) samples can retain 52%, 56%, and 58% at room temperature, respectively. Therefore, $K_3LaTe_2O_9$:Er is a good matrix material to achieve a stable DSL. The higher Er^{3+} ion concentration, the more obvious is the thermal quenching phenomenon of the sample. The thermal quenching mechanism of the luminescent material is usually different, containing ET, CR, and non-radiative transition.[26] The integrated intensity curves for various content samples have a similar slope. Thus, the ET rates between Er^{3+} ions causing heating temperature are similar. In addition, the probability of $^4S_{3/2}$ non-radiative relaxation to near-low energy level is small. Therefore, CR is mainly responsible for the luminescent thermal quenching.

According to Boltzmann's distribution, the intensity ratio (R_{HS}) between the thermal equilibrium levels of $^2H_{11/2}$ and $^4S_{3/2}$, (I_H/I_S), can be expressed as

$$R_{HS} = I_H/I_S = C \exp(-\Delta E/\kappa T), \quad (5)$$

where C is the constant relating to the host materials, ΔE is the energy gap between $^2H_{11/2}$ and $^4S_{3/2}$ levels, κ is the Boltzmann

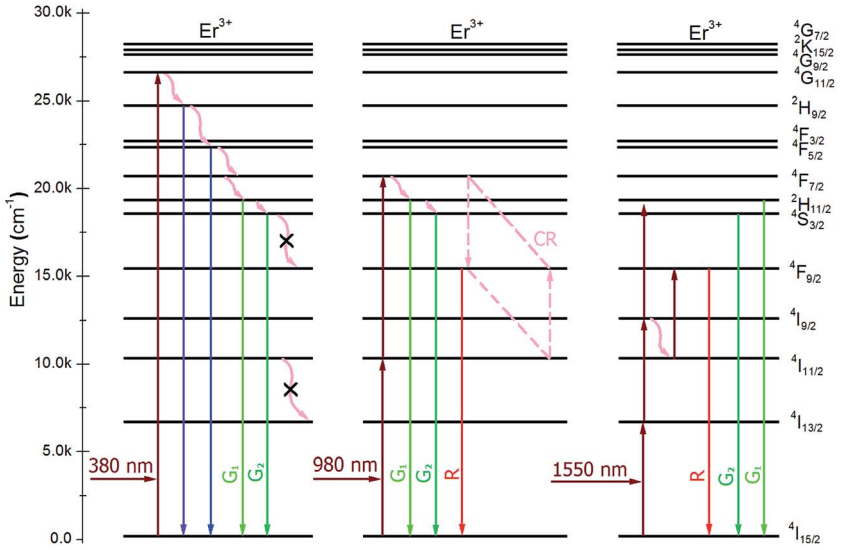

Fig. 6 Transition model of Er^{3+} ions in the $K_3LaTe_2O_9$ phosphor excited at 380, 980, and 1550 nm.

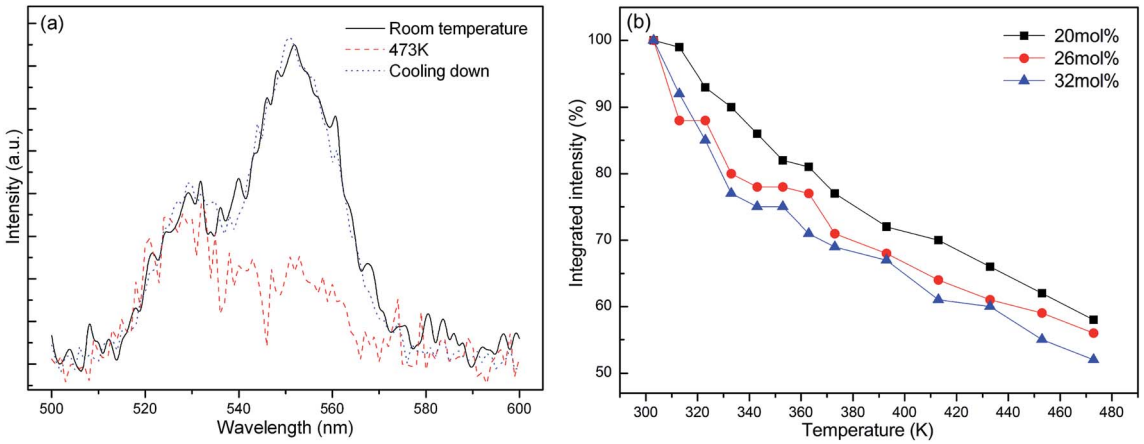

Fig. 7 DSL spectra of $K_3LaTe_2O_9$:0.26Er at different temperatures (a) and integrated emission intensities of $K_3LaTe_2O_9$:xEr phosphors as a function of temperature (b) (x = 20, 26, 32 mol%), (λ_m = 380 nm).

constant and T is the absolute temperature. The DSL spectra are adopted to characterise the temperature sensor properties and to avoid the thermal effect in UCL caused by the LD.[27] Eqn (5) was fit for the experimental data in Fig. 8a, and the curves for the $K_3LaTe_2O_9$:xEr samples from 303 K to 473 K (x = 20, 26, 32 mol%) were drawn. The fitting data show that the Er^{3+} ion concentrations affect the C and ΔE values. The R_{HS} values of $^2H_{11/2}$ and $^4S_{3/2}$ energy levels continuously enhance with increasing heating temperature, whereas the green DSL intensity decreases with increasing temperature. Sensitivity is an important parameter to evaluate the sensor performance for the temperature sensing. Sensitivity S can be derived according to eqn (6):

$$S = dR/dT = R(-\Delta E/\kappa T^2), \quad (6)$$

In general, the luminescence intensity caused by doping concentration exerts a slight effect on sensitivity. However, in the present study, the temperature sensitivity of the $K_3LaTe_2O_9$:Er samples decreases with increasing Er^{3+} ion concentration (Fig. 7b). This is due to that the change of the concentration of Er^{3+} ions may cause the change of the crystal field surrounding Er^{3+} ions, and the change of crystal field will cause the change of the optical transition rates of Er^{3+} ions. Therefore, the variation of radiation transition rate of $^2H_{11/2}$ and $^4S_{3/2}$ levels arouse the change of fluorescence intensity ratio FIR in different Er^{3+} ion doped samples and affect the sensitivity values. In addition, the thermal effects of samples is remarkable when concentration of doped Er^{3+} ions is higher.[28] The temperature of samples has an effect on crystal field. The sensitivities of 20 and 26 mol% Er^{3+} ions are similar, corresponding to approximately 0.008 and 0.0075 K^{-1} at 473 K, respectively. When the Er^{3+} ion concentration reaches 32 mol%, the sensitivity decreases rapidly, and its value is nearly 0.0057 K^{-1} (Fig. 8b). Therefore, the low Er^{3+} content should be carefully chosen to obtain the optimal sensitivity performance. The previously reports on temperature

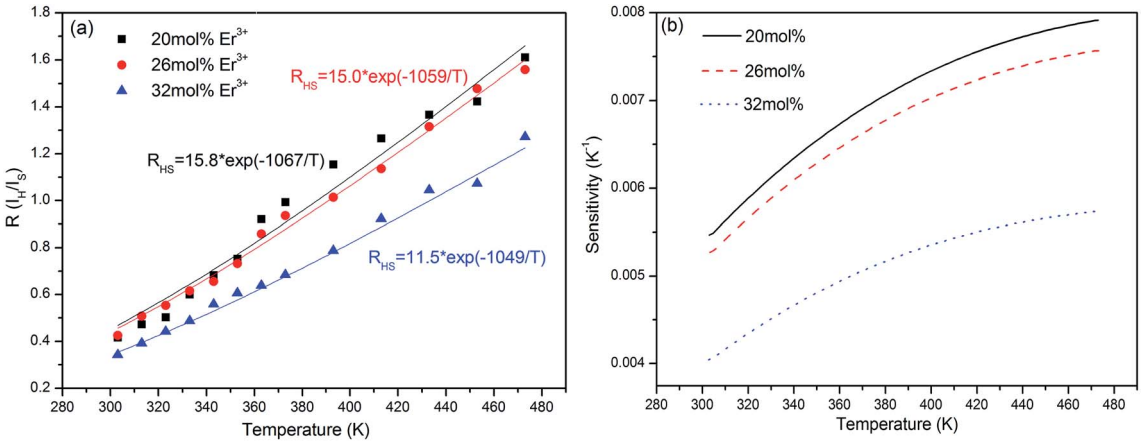

Fig. 8 Relationships between $^2H_{11/2}/^4S_{3/2}$ level green emission intensity radio and the heating temperature (a), and sensitivity curves of the $K_3LaTe_2O_9$:xEr samples (b) (x = 20, 26, 32 mol%).

sensitivities data were provided in Table S3.† On the basis of the experimental data in Fig. 8b, the $K_3LaTe_2O_9$:Er material can be used as the luminescent thermometer for temperature sensing. In addition, the above-mentioned results show that the Er^{3+} ion concentration is important to the thermal quenching and sensitivity of $K_3LaTe_2O_9$:Er phosphors.

4. Conclusion

A new green up-conversion luminescence material, $K_3LaTe_2O_9$:Er, was synthesised. The diffraction pattern of the hexagonal $K_3LaTe_2O_9$ crystal was indexed with Miller indices and the lattice constants $a = b = 0.60636 \pm 0.00018$ nm, $c = 1.49543 \pm 0.00037$ nm, and $V = 0.47617$ nm^3. The DSL and UCL properties of $K_3LaTe_2O_9$:Er were studied under 380, 980 and 1550 nm excitation. The shortest distance and average distance between Er^{3+} ions in the $K_3LaTe_2O_9$ matrix are significantly larger than that in normal phosphors. Therefore, energy migration is significantly suppressed, which is helpful in obtaining heavy Er^{3+} doping.

Acknowledgements

The authors thank the National Natural Science Foundation of China (No. 11504039 and 51502031), Liaoning Provincial Natural Science Foundation of China (No. 2015020206), and Research Program of Application Foundation (Main subject) of Ministry of Transport of PR China (No. 2015329225090). Fundamental Research Funds for the Central Universities (Grant Nos. 3132017061, 3132017066, and 3132016349) for their financial support. The authors thank Prof. Chang Liu for the XPS measurements.

References

1 H. Zheng, B. J. Chen, H. Q. Yu, J. S. Zhang, J. S. Sun, X. P. Li, M. Sun, B. N. Tian, H. Zhong, S. B. Fu, *et al.*, Temperature sensing and optical heating in Er^{3+} single-doped and Er^{3+}/Yb^{3+} codoped $NaY(WO_4)_2$ particles, *RSC Adv.*, 2014, **4**, 47556–47563.

2 Y. H. Zhang, L. X. Zhang, R. R. Deng, J. Tian, Y. Zong, D. Y. Jin and X. G. Liu, Multicolor Barcoding in a Single Upconversion Crystal, *J. Am. Chem. Soc.*, 2014, **136**, 4893–4896.

3 H. Dong, L. D. Sun, Y. F. Wang, J. Ke, R. Si, J. W. Xiao, G. M. Lyu, S. Shi and C. H. Yan, Efficient Tailoring of Upconversion Selectivity by Engineering Local Structure of Lanthanides in Na_xREF_{3+x} nanocrystals, *J. Am. Chem. Soc.*, 2015, **137**, 6569–6576.

4 T. Sasikala, L. Rama Moorthy and A. Mohan Babu, Optical and luminescent properties of Sm^{3+} doped tellurite glasses, *Spectrochim. Acta, Part A*, 2013, **104**, 445–450.

5 D. D. Yin, Y. W. Qi, S. X. Peng, S. C. Zheng, F. Chen, G. B. Yang, X. S. Wang and Y. X. Zhou, Er^{3+}/Tm^{3+} codoped tellurite glass for blue upconversion-structure, thermal stability and spectroscopic properties, *J. Lumin.*, 2014, **146**, 141–149.

6 M. M. Xing, Y. B. Ma, X. X. Luo, Y. Fu, T. Jiang, H. Wang and X. L. Duan, Design and achieving of multicolor upconversion emission based on rare-earth doped tellurite glasses, *J. Rare Earths*, 2014, **32**, 394–398.

7 G. Q. Chai, G. P. Dong, J. R. Qiu, Q. Y. Zhang and Z. M. Yang, 2.7 μm emission from transparent Er^{3+}, Tm^{3+} codoped yttrium aluminum garnet ($Y_3Al_5O_{12}$) nanocrystals–tellurate glass composites by novel comelting technology, *J. Phys. Chem. C*, 2012, **116**, 19941–19950.

8 M. Sobczyk and D. Szymanski, Optical properties of Sm^{3+}-doped $Y_2Te_4O_{11}$, *J. Lumin.*, 2015, **166**, 40–47.

9 W. S. Zhang and H. J. Seo, Luminescence and structure of a novel red-emitting phosphor Eu^{3+}-doped tellurate garnet $Li_3Y_3Te_2O_{12}$, *J. Alloys Compd.*, 2013, **553**, 183–187.

10 X. Y. Zhang, J. Y. Yao, X. X. Jiang, Y. Fu, Z. S. Lin, C. C. Zhang and Y. C. Wu, $K_3LaTe_2O_9$: a new alkali-rare earth tellurate with face-sharing TeO_6 octahedra, *Dalton Trans.*, 2015, **44**, 15576–15582.

11 B. P. Singh, A. K. Parchur and R. K. Singh, Structural and up-conversion properties of Er^{3+} and Yb^{3+} co-doped $Y_2Ti_2O_7$ phosphors, *Phys. Chem. Chem. Phys.*, 2013, **15**, 3480–3489.

12 A. N. Radhakrishnan, P. Prabhakar Rao, K. S. Mary Linsa, M. Deepa and P. Koshy, Influence of disorder to order transition on lattice thermal expansion and oxide ion conductivity in $(Ca_xGd_{1-x})_2(Zr_{1-x}M_x)_2O_7$ pyrochlore solid solutions, *Dalton Trans.*, 2011, **40**, 3839–3848.

13 P. Kubelka, New contributions to the optics of intensely light-scattering materials. Part I, *J. Opt. Soc. Am.*, 1948, **38**, 448–457.

14 Y. Tian, B. J. Chen, R. N. Hua, N. S. Yu, B. Q. Liu, J. S. Sun, L. H. Cheng, H. Y. Zhong, X. P. Li, J. S. Zhang, *et al.*, Self-assembled 3D flower-shaped $NaY(WO_4)_2$:Eu^{3+} microarchitectures: microwave-assisted hydrothermal synthesis, growth mechanism and luminescent properties, *CrystEngComm*, 2012, **14**, 1760–1769.

15 L. G. Van Uitert, Characterization of energy transfer interactions between rare earth ions, *J. Electrochem. Soc.*, 1967, **114**, 1048–1053.

16 J. J. Li, J. S. Sun, J. T. Liu, X. P. Li, J. S. Zhang, Y. Tian, S. B. Fu, L. H. Cheng, H. Y. Zhong, H. P. Xia, *et al.*, Pumping-route-dependent concentration quenching and temperature effect of green up- and down-conversion luminescence in Er^{3+}/Yb^{3+} co-doped $Gd_2(WO_4)_3$ phosphors, *Mater. Res. Bull.*, 2013, **48**, 2159–2165.

17 S. Fischer, B. Fröhlich, K. W. Krämer and J. C. Goldschmidt, Relation between Excitation Power Density and Er^{3+} Doping Yielding the Highest Absolute Upconversion Quantum Yield, *J. Phys. Chem. C*, 2014, **118**, 30106–30114.

18 G. H. Ju, Y. H. Hu, H. Y. Wu, Z. F. Yang, C. J. Fu, Z. F. Mu and F. W. Kang, A red-emitting heavy doped phosphor $Li_6Y(BO_3)_3$:Eu^{3+} for white light-emitting diodes, *Opt. Lett.*, 2011, **33**, 1297–1301.

19 X. M. Yin, H. Wang, M. M. Xing, Y. Fu, Y. Tian and X. X. Luo, Upconversion luminescence of $Y_2Ti_2O_7$:Er^{3+} under the 1550 and 980 nm excitation, *J. Rare Earths*, 2017, **35**, 230–234.

20 R. B. Anderson, S. J. Smith, P. S. May and M. T. Berry, Revisiting the NIR-to-Visible Upconversion Mechanism in β-$NaYF_4$:Yb^{3+},Er^{3+}, *J. Phys. Chem. Lett.*, 2014, **5**, 36–42.

21 M. T. Berry and P. S. May, Disputed Mechanism for NIR-to-Red Upconversion Luminescence in $NaYF_4$:Yb^{3+},Er^{3+}, *J. Phys. Chem. A*, 2015, **119**, 9805–9811.

22 L. A. Riseberg and H. W. Moos, Multiphonon orbit-lattice relaxation of excited stated states of rare-earth ions in crystals, *Phys. Rev.*, 1968, **174**, 429–438.

23 J. M. F. van Dijk and M. F. H. Schuurmans, On the nonradiative and radiative decay rates and a modified exponential energy gap law for 4f–4f transitions in rare-earth ions, *J. Chem. Phys.*, 1983, **78**, 5317.

24 X. L. Shen, M. M. Xing, Y. Tian, Y. Fu, Y. Peng and X. X. Luo, Upconversion photoluminescence properties of SrY_2O_4:Er^{3+},Yb^{3+} under 1550 and 980 nm excitation, *J. Rare Earths*, 2016, **34**, 458–463.

25 W. G. Yu, Y. Tian, M. M. Xing, Y. Fu, H. Zhang and X. X. Luo, Up-conversion luminescence of $NaY(WO_4)_2$:Yb,Er under 1550 and 980 nm excitation, *Mater. Res. Bull.*, 2016, **80**, 223–229.

26 B. N. Tian, B. J. Chen, Y. Tian, J. S. Sun, X. P. Li, J. S. Zhang, H. Y. Zhong, L. H. Cheng, Z. L. Wu and R. N. Hua, *Ceram. Int.*, 2012, **38**, 3537.

27 X. M. Yin, H. Wang, M. M. Xing, Y. Fu, Y. Tian and X. X. Luo, Up-conversion luminescence properties and thermal effects of $LaVO_4$:Er^{3+} under 1550 nm excitation, *Mater. Res. Bull.*, 2017, **86**, 228–233.

28 H. Wang, X. M. Yin, M. M. Xing, Y. Fu, Y. Tian, X. Feng, T. Jiang and X. X. Luo, Investigation on the thermal effects of $NaYF_4$:Er under 1550 nm irradiation, *Phys. Chem. Chem. Phys.*, 2017, **19**, 8465–8470.